Author Manuscript

Author Manuscript

Author Manuscript

Author Manuscript

HHS Public Access

Author manuscript

Eur J Med Chem. Author manuscript; available in PMC 2019 December 05.

Published in final edited form as:

Eur J Med Chem. 2018 December 05; 160: 193–206. doi:10.1016/j.ejmech.2018.10.009.

Identification and characterization of agnuside, a natural proangiogenic small molecule

Piyush Pillarisetti[a] and **Kenneth A. Myers**[b,*]

[a]Department of Biology, University of Pennsylvania, 433 S University Avenue, Philadelphia, Pennsylvania, 19104, USA ppiyush@sas.upenn.edu

[b]Department of Biological Sciences, 600 S 43rd Street, Philadelphia, Pennsylvania 19104, USA

Abstract

Due to its important role in regulating angiogenesis, vascular homeostasis and remodeling, and arteriogenesis in blood vascular and lymphatic endothelial cells, VEGFR2 stimulation has demonstrated promise in preclinical studies as an endovascular treatment for ischemic myocardial and peripheral disease. However, the short half-life of protein- and cytokine-based strategies and transduction inefficiency of vector-based modalities have hindered its clinical therapeutic applications. In the present study, we used a streamlined bioinformatics strategy combining ligand-based pharmacophore development and validation, virtual screening, and molecular docking to identify agnuside, a non-toxic, natural small molecule extract of *Vitex agnus-castus* possessing strong binding affinity, draggable physiochemical properties, and conformationally stable hydrogen bond and hydrophobic interactions with catalytically important residues within VEGFR2's active and allosteric sites. *In-vitro* proliferation, tube formation, and scratch wound migration assays provide evidence that agnuside promotes endothelial cell angiogenesis. Agnuside increases HUVEC proliferation with an EC_{50} of 1.376 μg/mL, stimulates tubulogenesis dose-dependently, and increases scratch wound migration rate. An additional angiogenesis assay suggests that agnuside may actively compete with a VEGFR2 inhibitor for VEGFR2 binding site occupancy to increase total length and branching length of HUVEC tubular networks. Chemometric analysis of molecular interaction fields (MIFs) by partial least squares (PLS)-derived quantitative structure activity relationship (QSAR) analysis and MIF contours provides the framework for the formulation of agnuside analogues possessing greater potency. Our research supports that agnuside may be a lead molecule for therapeutic angiogenesis.

Graphical Abstract

*corresponding author: Phone: 215-596-7531, Fax: 215-596-8710, k.myers@usciences.edu.

Publisher's Disclaimer: This is a PDF file of an unedited manuscript that has been accepted for publication. As a service to our customers we are providing this early version of the manuscript. The manuscript will undergo copyediting, typesetting, and review of the resulting proof before it is published in its final citable form. Please note that during the production process errors may be discovered which could affect the content, and all legal disclaimers that apply to the journal pertain.

Author Manuscript Author Manuscript Author Manuscript Author Manuscript

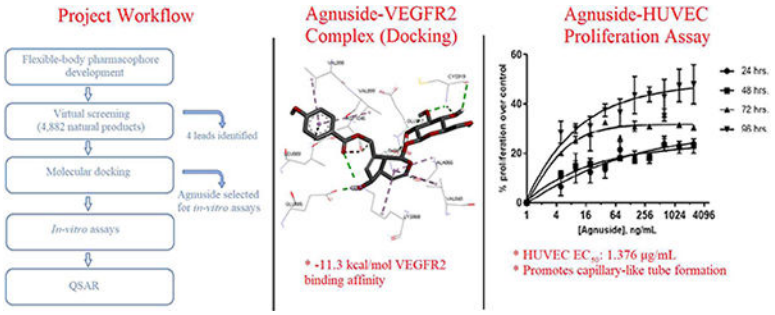

Keywords

Therapeutic angiogenesis; molecular modeling; drug discovery; agnuside; agonist; QSAR

Introduction

Blood vessel formation and remodeling are highly coordinated and spatiotemporal-based processes achieved by vasculogenesis, angiogenesis, and arteriogenesis. Angiogenesis, the stimulation of non-proliferative and quiescent endothelial cells in existing blood vessels by upregulation of hypoxia-inducible growth factors by tissue hypoxia, wound healing, ischemia, or inflammation, induces the formation of a new nascent blood vessel by endothelial cell migration and adhesion and subsequent capillary sprouting or intussusception [1]. Endothelial cell attachment, perivascular tissue invasion, and survival during sprouting requires the degradation of the subendothelial extracellular matrix (ECM) by endothelial cell-secreted ECM proteases, the formation of a provisional ECM composed of blood-born fibronectin, fibrinogen, and vitronectin, and regulation by substrate-ECM ligand-bound integrins and matricellular proteins [2]. Several proangiogenic cytokines contribute to these processes by responding to angiogenic cues and altering endothelial cell proliferation, integrin receptor expression, and production of secreted ECM proteins [2].

Binding interaction between vascular endothelial growth factor receptor-2 (VEGFR2) and vascular endothelial growth factor (VEGF) family members, including VEGFA-E and PLGF1–2, are important for proliferation of endothelial cells and their progenitors and for the formation of the provisional matrix during capillary sprouting [2–4]. VEGFR2 is a receptor tyrosine kinase with seven immunoglobulin homology domains, an intracellular split domain, and expression patterns in blood vascular and lymphatic endothelial cells [4]. VEGFR2's role in VEGF-stimulated angiogenesis and in maintaining vascular function homeostasis and adaptive cardiac growth by its vasodilatory and cardioprotective properties have made it a target for therapeutic angiogenesis [5–12]. Therapeutic angiogenesis can promote tissue regeneration and repair and wound healing by improving blood vessel collateralization and perfusion [12–13]. Several studies have also demonstrated its potential application for treating ischemic myocardial and peripheral diseases such as critical limb ischemia and coronary artery disease by revascularizing ischemic tissues affected by thrombotic occlusion [13–14].

Author Manuscript Author Manuscript Author Manuscript Author Manuscript

Therapeutic angiogenesis, which has largely been cell-based (transplantation of progenitor or precursor endothelial cells), protein-based (intravenous and intracoronary administration of rhVEGF), and gene-based (application of plasmid and adenoviral vectors), has had success in animal models, but limited success in humans [15–25]. Isner's phase I clinical trial [26] demonstrated that intramuscular delivery of $phVEGF_{165}$ in patients with peripheral Buerger's disease could result in newly visible collateral vessels and increased perfusion to ischemic limb. Makinen's phase II percutaneous transluminal angioplasty study [27] reported positive vascularity following VEGF gene therapy for ischemic lower-limb arteries. However, the majority of phase II/III therapeutic angiogenesis clinical trials for coronary and peripheral artery disease have yielded dissapointing results. Inefficacy of current modalities warrants identification of proangiogenic small molecules that stimulate vascular growth. Proangiogenic small molecules currently being investigated include ferric ion chelating agents such as FDA-approved deferoxamine that upregulates VEGF expression by intracellular HIF-1α stabilization and plant-derived pentacyclic triterpenes such as ursolic acid and β-amyrin that act on the Akt pathway [28]. Given the advancements made in structure-based drug design, pharmacophore modeling is often combined with molecular docking to identify lead molecules for biochemical evaluation, as described by Talele et al. [29]. Following biochemical evaluation, structural and chemical sites for improving small molecule potency are identified by QSAR analysis. Several studies have used computational drug-design processes to identify VEGFR2-interacting molecules [30–32]. Thus, an *in-silico* drug-discovery strategy was used to identify and characterize a non-toxic, natural small molecule possessing VEGFR2 agonism and druggable physiochemical properties.

Material and Methods

Data set collection and structural optimization

In order to identify lead compounds possessing strong binding affinity and conformational stability with VEGFR2, a collection of naphthamides reported by Harmange et al. [33] composed of dimethoxyquinoline and oxynaphthalene motifs and a carboxamide-linked aromatic group was used as a dataset for the computational procedures. All compound structures were retrieved from NCBI PubChem database. The naphthamides are structurally optimal for lead molecule identification by their aromatic ring systems and torsional flexibility. Naphthamides were subjected to partial charge assignment, torsional angle parameterization, and bond length/angle parameterization using the general AMBER force field [34]. HF/6–31G* charges were assigned to all non-standard residues using the Restrained Electrostatic Potential (RESP) method in AMBER Antechamber module [35]. Conjugate gradient minimization for 10 steps and with a 0.02 Å conjugate gradient step size was performed to relieve highly unfavorable clashes within the molecules and to find local energy minimum states. Partial charge assignment, geometry optimization, and energy minimization were performed using UCSF Chimera [36]. The crystal structure of the VEGFR2 extracellular kinase domain in complex with N-(4-chlorophenyl)-6-(6,7-dimethoxyquinoline-4-yl)oxynaphthalene-1-carboxamide was retrieved from the RCSB Protein Data Bank (PDB ID: 3B8Q, 2.75 A). Protein optimization was performed by deleting the solvent and ligand, replacing incomplete side chains using the dunbrack rotamer library, assigning appropriate protonation states for histidine, and adding hydrogens. Energy

Author Manuscript Author Manuscript Author Manuscript Author Manuscript

minimization was performed for 100 steepest descent minimization steps with 0.02 Å steepest descent initial step size and 10 conjugate gradient minimization steps with 0.02 Å conjugate gradient step size. Protein optimization and minimization were performed using UCSF Chimera.

Pharmacophore modeling

Pharmacophore model generation and validation were performed using LigandScout 3.1. [37] to relate the binding affinities of the series of chemically diverse VEGFR2-binding naphthamides with their physicochemical properties. Pharmacophoric development requires a training set for molecular alignment and superpositioning and a structurally diverse test set for external scoring and validation. To accomplish this, the dataset was divided into 6 training set compounds possessing the same core oxynaphthalene starting scaffold (A) and −6,7-dimethoxyquinoline motif, but different chemical substituents on the R_2 carboxamide-linked aromatic group and different VEGFR2 binding affinities, and 23 test set compounds of three scaffolds (A-C) with related structural elements (Table 1). Because local minimum energy states of molecules do not represent their structure within the receptor's binding cavity, the VEGFR2-bioactive conformation of NAPH1, 6-(6,7-dimethoxyquinoline-4-yl)-oxy-N-phenylnaphthalene-1-carboxamide, was determined by AutoDock Lamarckian Genetic Algorithm (GA) molecular docking routines and used as the template molecule for flexible, atom-based molecular superpositioning of the other energy minimized training set compounds. Marvinview [38] was used to create five additional conformers of the NAPH1 bioactive structure with MMFF94 forcefield, normal optimization limit parameters, and a diversity limit of 0.2 A to preserve the bioactive integrity of the structure. Interaction patterns for positive ionizable, negative ionizable, hydrophobic, hydrogen bond donor, and hydrogen bond acceptor groups were used for ligand-based common pharmacophore hypothesis (CPH) generation. To create consensus models, merged-feature, instead of shared-feature, CPHs were constructed using pharmacophore fit/atom overlap scoring function, a feature tolerance scale factor of 1.00, and 10.0% threshold for partially matching features. Exclusion volumes were also computed during model development.

Decoy set validation and virtual screening

2D descriptor-based decoy set validation was performed to assess the predictive ability and statistical significance of the merged-feature pharmacophores and to determine which to use for ligand-based virtual screening. The basis of external decoy set validation is to screen a compound database consisting of active molecules known to bind VEGFR2 and molecular descriptor-based decoy molecules that share similar chemical properties as the actives, but a dissimilar structural topology. Sixteen naphthyl-based molecules with strong VEGFR2 binding affinity were used as actives and 1,595 molecular descriptor-based decoys with an active ligand versus tanimoto threshold of 0.75 (ensuring chemical diversity between the active ligands and decoys), decoy versus decoy tanimoto threshold of 0.90 (ensuring chemical diversity amongst the decoys), active ligand hydrogen bond acceptor variance of ±2, hydrogen bond donor variance of ±1, molecular weight variance of ±25 Da, rotational bond variance of ±1, and logP variance of ±1 were identified and retrieved from ZINC chemical database using DecoyFinder 2.0 [39]. The 1,611 compound decoy set was screened against the generated CPHs and various statistical parameters including total hits, active hits,

Author Manuscript Author Manuscript Author Manuscript Author Manuscript

false negatives, false positives, enrichment factor, and percent yield-ratio of actives were calculated. The pharmacophore with the strongest external decoy set validation parameters and highest test set pharmacophoric fit scores were used for ligand-based virtual screening of the AnalytiCon Discovery MEGx natural purified compounds of microbial and plant origin database.

Molecular docking

Molecular docking of the naphthamides and lead compounds identified by virtual screening (agnuside, erythro-anethole glycol 1-glucoside, sachaliside, and rosin) with VEGFR2 was performed using AutoDockTools 1.5.6 [40]. AutoDock performs automated molecular docking using a Lamarckian genetic algorithm and uses an empirical binding free energy force field to compute binding constants of ligand-protein complexes. Polar hydrogens, atom-based solvation parameters and fragmental volumes, and Kollman United Atom charges were added to the VEGFR2 RTK crystal structure, and non-polar hydrogens were merged. Polar hydrogens and Gasteiger charges were added to each ligand. To account for torsional degrees of freedom during GA evaluation, the number of rotatable bonds was designated for each ligand. The docking site was defined by a grid-box surrounding all residues within 10 Å of ATP binding site, and AutoDockTools assigned pair-wise potential parameters (Lennard-Jones 6–12 potential and equilibrium internuclear separation/energy well depth parameters) to the energy descriptor fields describing the ligands' atom types. Electrostatic parameters were also computed. Default parameters were used for grid-box creation: 40×40×40 grid points with 0.375 Å spacing. Glu885 was subjected to sidechain flexibility to account for receptor flexibility during protein-ligand interaction and to improve VEGFR2 docking [41]. Darwinian GA and Lamarckian GA docking-search parameters were applied for 50 runs and population size of 50. A maximum of 3.5 mil. evaluations and 27k generations was specified with 0.02 gene mutation rate, 0.80 crossover rate, and 1.00 variance of Cauchy distribution for gene mutation. RMS cluster tolerance for the top-scored docked configurations was set to 1.00 Å. The following molecular mechanics terms were computed using AutoDock's empirical binding free energy function: $E_{electrostatic}$ (electrostatic energy) and $E_{vdw+Hbond+desol}$ (van der Waals, hydrogen bonding, and desolvation energies). $E_{electrostatic}$ is calculated using a screened Coulombic electrostatic potential. E_{vdw} is calculated using a Lennard-Jones 6–12 dispersion repulsion interaction term based on Amber force field. E_{Hbond} is calculated using a directional 10–12 hydrogen bonding term based on probe-target atom angle. $E_{desolvation}$ measures hydrophobicity effects caused by solvent entropy changes at solute-solvent contacts using a volume-summing method. The desolvation term is weighed by an atomic solvation parameter for each atom type and a docked ligand desolvation estimate. Docked complexes were visualized in Discovery Studio 4.0 Client [42] and atom connectivity of Glu885 was amended.

3D-QSAR model development

Three-dimensional quantitative structure-activity relationship (3D-QSAR) model development was performed using Open3DQSAR software [43]. Docking-based, instead of multifit alignment-based, 3D-QSAR models were developed by enclosing the bioactive conformations of nineteen naphthyl-based compounds, including those of the pharmacophore development training set, in a 1.00 Å step grid-box with 5.00 Å outgap. The

Author Manuscript Author Manuscript Author Manuscript Author Manuscript

bioactive structures were extracted from docking complexes. Steric (Lennard-Jones 6–12 potential) and electrostatic (Coulombic potential) molecular interaction fields (MIFs) within the grid-box were generated using a carbon probe atom and a volumeless probe with a +1 charge, respectively. Binding energies of the nineteen compounds calculated by AutoDock were used as dependent variables in 3D-QSAR evaluation. A series of pre-treatment modifications were made to improve computational efficiency and to derive stronger field properties for partial least squares (PLS) analysis. The electrostatic potential energy values within the naphthamides were subjected to steric cutoff of 10,000 kcal/mol and the energy cutoff values for principal component (PC) extraction were set to 20.0, 30.0, and 40.0 kcal/mol. MIF energy values less than 0.05 kcal/mol were zeroed. The series of nineteen naphthamides were split into a training set of 16 and test set of 3. Test set molecules possessed diverse binding affinities, ranging from −12.05 to −14.33 kcal/mol. In order to allocate equitable importance to all field descriptors and reduce the chance of biased PC extraction, MIF variables with standard deviations less than 0.10 and N-level variables were eliminated from computation, and block unscaled weighting for both fields was performed by assigning collective block weighting coefficients. In order to identify the optimal number of PCs for PLS regression analyses, different cross validation (CV) strategies, including leave-one-out, leave-two-out, and leave-multiple-out, were performed with variable grouping and selection parameters using the in-built Smart Region Definition and Fractional Factorial Design algorithms. QSAR model validation requires training set internal validation and randomized external validation [44]. The cross-validated correlation coefficient (q^2) for each CV strategy was computed. Final PLS regression models after variable selection by CV were built and non cross-validated correlation coefficient (r^2), non cross-validated predicted correlation coefficient for test-set (r_{pred}^2), F-test value, SDEC, standard deviation of error of prediction for non cross-validated training set (SDEP), and standard deviation of error of prediction for cross-validated test set ($SDEP_{test}$) were computed. The optimal number of components for scaffold optimization of agnuside was chosen based on strongest q^2 for all CV strategies and r^2 values. PLS field coefficients for the optimal number of PCs were exported as grid maps and visualized in PyMOL [45].

Cell culture and reagents

Human umbilical vein endothelial cells (HUVECs) were maintained in endothelial basal media (EBM; Lonza) and supplemented with 5% fetal bovine serum (FBS), 0.4% bovine brain extract (BBE), 0.1% human epidermal growth factor (HEGF), and 0.1% hydrocortisone, and grown at 30° C in 5% CO_2 atmosphere. Cells seeded at $3–5\times10^5$ cells/T75 flask in 5% FBS complete EBM media reached 90% confluency within 3–4 days. The confluent cell monolayer was washed with phosphate-based saline (PBS) and trypsinized with 0.5% trypsin inhibitor. All functional characterization assays were performed with P5–8 HUVECs. Agnuside (>95% pure) was purchased from Sigma (St. Louis, MO, USA), dissolved in DMSO, and maintained at −20° C as a stock solution. Carrier free recombinant human $VEGF_{165}$ was purchased from BioLegend (San Diego, CA, USA), vortexed and aliquoted, and maintained at −20° C. The VEGFR2 inhibitor ZM 323881 HCl (VEGFR2 IC_{50} < 2nM) was purchased from Selleck, dissolved in DMSO, and maintained at −20° C.

Author Manuscript Author Manuscript Author Manuscript Author Manuscript

HUVEC proliferation assays

Agnuside and VEGF induced proliferation assays were performed by seeding 5×10^4 HUVECs in 100 μl of 5% FBS EBM complete media into each well of a 96-well tissue culture plate. After 24 hr. incubation, complete media was removed and replenished with either 100 μl 5% FBS EBM complete media containing various concentrations of the rhVEGF (0.10–256 ng/mL) or agnuside alone (1.00–2500 ng/mL). 0.020% DMSO concentration for all the agnuside treatments was maintained. Relative proliferation as percentage proliferation over control was measured at different time points (24–96 hrs.). At each time point, HUVECs were treated with 20 ng/mL DAPI under the same conditions. After 20 min. incubation, plates were read at 530/590 nm emission/excitation using a microplate spectrofluorometer. Proliferation assays were performed in duplicate.

Angiogenesis assays

Functional characterization of agnuside by evaluating its effects on HUVEC migration and tube formation was performed by agnuside-induced angiogenesis assays. An additional angiogenesis assay was performed as a competitive ligand experiment to understand agnuside's receptor-mediated mechanism of action and to assess whether agnuside may actively compete with a highly selective VEGFR2 inhibitor in modulating VEGFR2 activity. 30 μl of growth factor-reduced Geltrex (Thermo Fischer Scientific) was applied to the bottom of each well of a 96-well tissue culture plate and allowed to incubate and polymerize for 30 mins. To determine whether agnuside affects the extent of angiogenesis, 100 μl of 5% FBS EBM complete media containing different concentrations of agnuside (0.01–600 ng/mL) and 3×10^4 HUVECs were added to each well. For the competitive ligand experiment, 100 μl of 5% FBS EBM complete media containing 0.1 ng/mL agnuside, 1 nM ZM 323881 HCl VEGFR2 inhibitor, DMSO vehicle, or 0.1 ng/mL agnuside plus 1 nM ZM 323881 HCl with 3×10^4 HUVECs were added to each well. For the 0.1 ng/mL agnuside plus 1 nM ZM 323881 treatment, 0.1 ng/mL agnuside was added to HUVECs initially and allowed to incubate for 30 minutes. 1 nM ZM 323881 HCl was added after 30 min. incubation to allow agnuside to occupy its target receptor's active site. By pre-treating HUVECs with agnuside and subsequently adding ZM 323881 HCl, agnuside and ZM 323881 HCl could compete with each other for VEGFR2 binding site occupancy. ZM 323881 HCl has a VEGFR2 IC_{50} <2 nM so off-target effects of the inhibitor were minimal. Plates were incubated for 22 hours. 4x and 10x phase-contrast images were acquired at 22 hrs for each condition and tube formation, measured by total meshes area, total length, and total branching length, was measured using Angiogenesis Analyzer of ImageJ. Angiogenesis assays were performed in duplicate.

HUVEC migration assays

The rate of scratch wound-induced HUVEC planar migration in the presence of agnuside was measured by plating 5×10^4 HUVECs in 100 μl EBM complete media in each well of a 96-well tissue culture plate. After confluent monolayers were formed, media was removed, cells were lightly washed with PBS, and linear scratches were made through the center of the wells using a 10 μl pipette. Wells were viewed under phase-contrast microscope to ensure uniformity of scratches. 100 μl complete media containing different concentrations of

Author Manuscript Author Manuscript Author Manuscript Author Manuscript

agnuside (0.01–600 ng/mL) were added to each well. After 24 hrs., media was removed and 4x phase-contrast images of each treated well were taken. The rate of scratch wound migration was measured at 5 randomly selected locations along the scratch wound for each treatment using ImageJ. Migration assays were performed in duplicate.

Results and Discussion

3.1. Ligand-based pharmacophore modeling

To determine chemical functionalities and steric properties required for small molecules to interact with VEGFR2 with strong binding affinity, five substructure-based CPHs were determined using the training set of six naphthyl-based derivatives and 24 test set molecules. Superpositioning of the bioactive conformation of template molecule NAPH1 derived from the Lamarckian GA routine with energetically-minimized structures of NAPH2–6 from molecular alignment is shown in Fig. 1a, b. CPHs were developed using the following chemical features: aromatic ring (**AR**), hydrogen bond acceptor (**HBA**), hydrogen bond donor (**HBD**), positive ionizable (**P**), negative ionizable (**N**), and hydrophobic group (**H**). Five high scoring CPHs were constructed and scored by structural fit. *CPH1* and *4* are shown in Fig. 1c, d with NAPH1's aligned bioactive structure. *CPH1* indicated the importance of an aromatic ring system near the solvent-accessible −6,7-dimethoxyquinoline motif at R_1 position; hydrogen bond acceptors extending from R_1 substructure into the hydrophobic groove near VEGFR2's front pocket; and hydrophobic substituents adjacent to the oxynaphthalene substructure. All five CPHs contained the three chemical features: **AR**, **HBA**, **H**. *CPH1–3* contained three **AR**, three **HBA**, and two **H**. Minor steric differences between them were due to variation in planar directionality of the dimethoxyquinoline aromatic groups, suggesting different means of access to the front pocket. No shared chemical functionalities exist among the CPHs near R_2 substituent because the carboxamide linker permits torsional flexibility of the adjacent phenyl or isoxazole groups within the extended back pocket, suggesting the importance of scaffold A's -N and =O positions. *CPH1* possessed the highest pharmacophoric fit score: 0.8864. *CPH4* had a 0.8190 fit score and contained three **AR**, four **HBA**, and three **H**. NAPH1 possessed the highest pharmacophoric fit score (94.59) with *CPH4* and contained all its feature patterns. As shown in Fig. 1e, f. there are two **H** and two **AR** near *CPH4's* oxynaphthalene substructure and a **HBA** at =O position of the carboxamide linker, a chemical feature overlap not observed in other CPHs. *CPH5* had the lowest score (0.7902) and contained one **AR**, one **HBD** (NH of carboxamide linker), and two **H**. The developed CPHs are in good agreement with molecular docking results and indicate the importance of VEGFR2-binding molecules to form hydrogen bond and hydrophobic interactions with the active site and tunnel region of the receptor surface, respectively.

3.2. Decoy set validation and ligand-based virtual screening

In addition to test set scoring, the predictive ability of the best pharmacophore hypothesis *CPH1* was assessed using an external 2D-descriptor based decoy set of molecules which shared similar chemical features as the active molecules (number of HBA, HBD, rotatable bonds, molecular weight, and logP), but dissimilar structural topology. The total number of molecules in the generated decoy set database (D) was 1,611 and the total number of actives

Author Manuscript Author Manuscript Author Manuscript Author Manuscript

was 16. *CPH1* had the highest enrichment factor (0.891) of the CPHs and identified 56.3% of total actives with a false positive percentage of 0%, indicating the specificity of the developed pharmacophore (Table 2a). Although the percent ratio of actives in the hit list was <38% for the remaining CPHs, all models had 0% false positives. Because of its strong predictive ability, *CPH1* was screened against the 4,882 compound-MEGx database of natural purified microbial and plant extracts. Four lead molecules (0.08% hit rate): agnuside, erythro-anethol glycol 1-glucoside, sachaliside, and rosin satisfied six pharmacophoric features of *CPH1* and were considered for further molecular docking analysis. Agnuside, a non-toxic iridoid glycoside extracted from *Vitex agnus-castus,* possessed the highest pharmacophoric fit score (66.82) of the lead molecules and satisfied *CPHTs* **AR** defined by scaffold A naphthamides' oxynaphthalene core structure, 3 **HBA**, and 2 **H**, chemical functionalities required for stabilization in the tunnel region and solvent-accessible front pocket of VEGFR2. None of the lead molecules mapped to the **AR** groups defined by the dimethoxyquinoline motif of the naphthamides. Pharmacophoric fit score and matching features of the lead molecules and their *CPH1* overlap are shown in Table 2 and Fig. 2. Agnuside, erythro-anethol glycol 1-glucoside, sachaliside, and rosin possess chemical and steric favorability for angiogenic modulation.

3.3. Molecular docking

To understand the interaction mechanisms between the naphthyl-based compounds used in pharmacophore generation and the VEGFR2 binding site, molecular docking was performed in AutoDock using Lamarckian GA. Global minimum-energy configurations of the complexes indicate that the strong binding affinity of the naphthamides is due to (*i*) carboxamide-linked aromatic groups interacting with a hydrophobic ligand binding pocket; (*ii*) short-range hydrogen bonding between the -NH of carboxamide linker and the Glu885 backbone, as suggested by *CPH5*; (iii) electrostatic and van der Waals interactions between the oxynaphthalene substructure and the kinase hinge region; and (iv) hydrophobic network formation between the aromatic ring structures of −6,7-dimethoxyquinoline and the ATP binding pocket.

The binding, electrostatic, van der Waals, hydrogen bond, desolvation, and total internal energies contributing to binding interactions between VEGFR2 and NAPH1–19 and lead molecules, along with distances of several important hydrophobic interactions with catalytically important residues in the kinase hinge region, tunnel region, and back pocket are described in Table 4. Contrary to the *CPH1* model, scaffold A naphthamides that project into the solvent accessible cavity surrounding Lys868 are stabilized by a hydrophobic bond between the R_2 substituent and the isobutyl sidechain of Leu889 (~4.829 A), thereby situating NH of carboxamide linker within H-bonding distance of Glu885 and Asp1046 sidechains. Oxynaphthalene moieties of training set molecules NAPH1 and 4–6 all form a cation-n electrostatic bond with the a-amino group of Lys868 (~4.580 Å) and several hydrophobic interactions with proximal residues, stabilizing the core structure within the tunnel region. Consistent with *CPH1,* the aromatic ring systems of the dimethoxyquinoline extend into the hydrophobic groove of the front pocket, defined by Leu840, Ala866, Glu917, Phe918, Cys919, Lys920, and Leu1035. The template molecule used in pharmacophore development, NAPH1, had the highest binding and total internal component energies

Author Manuscript Author Manuscript Author Manuscript Author Manuscript

(−15.00 and −3.68 kcal/mol, respectively) of the training set molecules. NAPH1-VEGFR2 complex is shown in Fig. 3 with hydrophobicity and solvent-accessible surface (SAS) potential maps.

Lead molecules identified by virtual screening were also docked into the VEGFR2 active site to determine their binding orientations. Agnuside occupies a similar orientaton as the naphthamides within the binding groove and possesses a −11.28 kcal/mol binding energy, the lowest of the lead molecules. Electrostatic interactions between agnuside-VEGFR2 are not critical, as indicated by a −0.08 kcal/mol electrostatic component. As shown in Fig. 4a, agnuside's 4-hydroxyphenyl moiety is involved in a hydrophobic network with the sidechains of Leu889 (3.628 Å) and Val899 (5.416 Å and 5.441 Å). C=O of its carboxylic linker acts as a hydrogen bond acceptor to -NH_3 of Lys868 (2.636 Å) and Asp1046 sidechains (2.558 Å) (Fig. 4a). The hydroxyl group attached to the cyclopentane substructure acts as a hydrogen bond donor to Glu885 (1.911 Å) and the adjacent pyran forms several hydrophobic bonds with Lys868, Val848, and Ala866 (4.827 Å, 4.894 Å, and 4.255 Å, respectively), as predicted by *CPH1.* Atom-specific affinity maps for carbon and oxygen confirm that the cyclopentane-pyran substructure is in pockets of carbon and oxygen affinity. Hydroxyl groups on the O-linked glucose moiety are involved in several hydrogen bonds with Thr916, Glu917 and Cys919 (Fig. 4a). To improve the binding affinity of agnuside, hydrophobic stabilization may be achieved by substituting cyclopentane-pyran with a benzimidazole or isoindole group. The strong binding affinity of agnuside is due to hydrophobic and hydrogen bond network formation with surrounding receptor atoms. As shown in Fig. 4d, the O-linked glucose moiety of erythro-anethole glycol 1-glucoside actes as both a hydrogen bond donor and acceptor to the Cys919 sidechain and the 1-(4-methoxyphenyl) group forms a n-n stacked hydrophobic bond (4.180 Å) with aromatic ring of Phe1047. The methoxyphenyl group does not occupy the extended hydrophobic pocket or tunnel region due to torsional rigidity of the ether linker, thus failing to interact with catalytically important residues (Fig. 4d). As a result, erythro-anethole glycol 1-glucoside has a - 6.460 kcal/mol binding energy with desolvation, van der Waals, and H-bond energies accounting for - 4.84 kcal/mol. Rosin and sachaliside, structurally similar to erythro-anethole, have improved binding energies (−9.270 and −9.740 kcal/mol, respectively) and are less exposed to solvent due to modification of the linker between their phenyl and glucose groups (Fig. 4g, j). Based on hydrogen bond and hydrophobic network formation and binding free-energy calculations, agnuside possessed the best physicochemical properties for *in-vitro* studies. The structure of agnuside is shown in Fig. 5.

3.4. 3D-QSAR development by PLS analysis

To determine how the physicochemical properties of the naphthamides relate to their binding affinity and to identify regions of steric and electrostatic favorability on the receptor surface, chemometric analysis of the MIFs surrounding their bioactive conformations was performed. Docked configurations of the training and test set molecules were used for several pre-treatment modifications, ensuring the reliability of QSAR-derived coefficient contour maps. PLS analysis with 3 PCs and 30.0 kcal/mol energy cutoff resulted in a QSAR model with cross-validated q^2 values of 0.777 (leave-one-out), 0.753 (leave- two-out), 0.736 (leave-multiple-out), non cross-validated r^2 of 0.961, and variance F of 98.19, ensuring the model's

Author Manuscript Author Manuscript Author Manuscript Author Manuscript

internal predictability. The r^2 for external test set prediction, r_{test}^2, was 0.933 with a corresponding standard error of prediction ($SDEP_{test}$) of 0.256, indicating the model's fitting power and external predictability. External predictability, measured by cross-validated correlation coefficients and the standard deviation of error of prediction for test set molecules, and internal predictability, measured by r^2 and $rpred^2$, were strongest for the 3 PC extraction-PLS analysis with 30.0 kcal/mol energy cutoff. Calculated versus actual binding energies for leave-one-out CV for training and test set molecules are described in Fig. 6. Statistics of PLS analysis for 1–6 PCs at 1.00 Å step size and at 20.0, 30.0, and 40.0 kcal/mol energy cutoffs are shown in Table 5. Visualization of the steric and electrostatic MIFs was performed using the QSAR-derived 3 PC 30.0 kcal/mol energy cutoff model.

3.5. 3D-QSAR steric and electrostatic contour maps

QSAR-derived coefficient contour maps, defined by important steric and electrostatic field properties of the naphthamides, are shown in Fig. 7 with the bioactive conformations of NAPH1 and agnuside. Green and yellow contours represent regions where steric bulkiness improves and reduces binding affinity, respectively, whereas blue and red contours represent regions where electropositive species improve and reduce binding affinity, respectively. The isosurf value of the van der Waals MM coefficient field was ±0.0003. The green contours proximal to agnuside's 4-hydroxyphenyl indicate that bulky substituents on its carboxylic ester and hydroxyphenyl groups may improve component interaction energies with VEGFR2's tunnel region and back pocket. The receptor SAS potential complements the computed van der Waals field properties as the solvent-accessible hydrophobic back pocket may accommodate substitution of the hydroxyphenyl with bulkier groups. For naphthamides, bulky substituents on the carboxamide-linked aromatic groups in this region propagate hydrogen bond and hydrophobic network formation. Three yellow contours adjacent to agnuside's cyclopentane-pyran substructure suggest that bulkiness of its hydroxyl groups reduces stability within the tunnel region. A yellow contour is also situated near the glucose moiety of agnuside. Comparing NAPH7 and 11 with other training set naphthamides indicates that bulky substituents such as chlorophenyl in this region disfavor affinity. The isosurf value for the electrostatic MM coefficient field was ±0.0001. The large blue contour region surrounding the hydroxyl groups of agnuside's glucose moiety suggests the addition of electropositive substituents in this region. Mapping the hydrogen bond surface potential with these field values reveals complementarity, as the NO and CO sidechains of Thr916, Glu917, and Cys919 can serve as HBAs. Five regions of red contour surround agnuside's hydroxyphenyl motif, suggesting that electronegative substituents improve conformational stability in this region. Taken together, suitably bulky, hydrophobic, and electronegative substituents on agnuside's carboxylic ester and 4-hydroxyphenyl, and sterically-restricted, electropositive substituents on the cyclopentane-pyran and glucose substructures may improve agnuside's binding affinity.

3.6. Agnuside exerts pro-angiogenic effects on HUVEC proliferation, tube formation, and migration

HUVEC proliferation in the presence of all tested agnuside concentrations (1–2500 ng/mL) at all time points (24–96 hrs.) was markedly higher than in DMSO control. Up to a 56% increase in HUVEC proliferation was measured for 2500 ng/mL agnuside treatment at 96

Author Manuscript Author Manuscript Author Manuscript Author Manuscript

hrs., compared to a 20–30% increase for 24–72 hrs., shown in Fig. 8a. Agnuside's measured EC_{50} at 96 hrs. was 1.376 pg/mL. No differences in cell morphology were observed for any treatments. As shown in Fig. 8b, VEGF promoted HUVEC proliferation in a similar time- and dose-dependent manner and possessed greater potency than agnuside with a 96 hrs. EC_{50} of 1.274 ng/mL. To understand agnuside's effect on HUVEC angiogenesis, total meshes area of the agnuside-treated tubular networks was measured. Total meshes area represents the area occupied by the primary capillary-like tubes. Total length represents the sum of the lengths of capillary-like branches, isolated elements, and segments and total branching length represents the sum of length of trees composed from segments and branches. Agnuside promoted formation of meshes in a dose-dependent manner. At 22 hrs., a significant increase in total meshes area was observed for HUVECs treated with 1.00 ng/mL agnuside compared to DMSO control and nonsignificant increases were observed for 0.1 and 10 ng/mL agnuside treatments (Fig. 8c). As shown in Fig. 8d, e, 0.1 ng/mL agnuside appears to compete with ZM 323881 HCl at 22 hrs. for the VEGFR2 binding site. Total length and total branching length of 0.1 ng/mL agnuside-treated HUVEC tubular networks were greater than DMSO control. Total length and total branching length for 0.1 ng/mL agnuside plus 1 nM ZM 323881 HCl-treated HUVECs were less than for 0.1 ng/mL agnuside alone but greater than for 1 nM ZM 323881 HCl alone. Even in the presence of 1 nM ZM 323881 HCl, 0.1 ng/mL agnuside resulted in greater total length and total branching length compared to DMSO control. The data may suggest that agnuside exerts a proangiogenic effect on HUVECs by competing with ZM 323881 HCl for VEGFR2 binding site occupancy. As shown in Fig. 8g, HUVEC wound closure 24 hrs. after initial scratch wound application was accentuated in the presence of 100 ng/mL agnuside relative to control.

Conclusions

In the present study, we identified a nontoxic, natural small molecule possessing strong binding affinity and conformational stability with VEGFR2 in molecular docking models and subsequently characterized the molecule as proangiogenic by *in-vitro* HUVEC assays. Our research provides evidence that agnuside extract derived from *Vitex agnus-castus* stimulates angiogenic processes. Many preclinical studies have demonstrated that angiogenic stimulus to ischemic areas improves blood vessel collateralization and perfusion. However, the suboptimal results of many clinical trials in humans have challenged the application of therapeutic angiogenesis and have created concern about the efficacy and delivery mechanisms of protein- and gene-based modalities. Localized administration of proangiogenic small molecules is of active research and such administration to areas of angiogenic deficiency may improve the utility of therapeutic angiogenesis.

Pharmacophore modeling using VEGFR2-binding naphthamides and virtual screening of a natural compound database resulted in the identification of four lead molecules with the appropriate chemical and structural features to interact with VEGFR2's binding site. Molecular docking indicated that agnuside, by its strong hydrogen bond and hydrophobic network interactions with the VEGFR2 front and back pockets, possessed the strongest binding affinity (−11.28 kcal/mol) of the lead molecules. HUVEC proliferation, angiogenesis, and migration assays demonstrated that agnuside increases HUVEC

Author Manuscript Author Manuscript Author Manuscript Author Manuscript

proliferation in a time- and dose-dependent manner, stimulates tube formation at 0.10–10 ng/mL, and accelerates scratch wound migration at 100 ng/mL. The reason why only 100 ng/mL agnuside induces such a pronounced increase in the rate of scratch wound migration is unclear and needs further investigation. An angiogenesis assay designed to evaluate binding competition between agnuside and ZM 323881 HCl suggests that agnuside may compete with the inhibitor for VEGFR2 binding site occupancy to exert pro-angiogenic effects on HUVECs, supporting *in-silico* results. In addition, chemometric analysis of steric and electrostatic MIFs surrounding agnuside's bioactive structure provides information about SAR modifications to improve agnuside's potency. The computational development and synthetic feasibility of agnuside analogues will be further investigated.

Acknowledgements

We thank the University of the Sciences for providing research space and equipment necessary to conduct the described experiments. This work was supported by funding from the National Institutes of Health to K.A.M. (grant #: K22HL113069).

Abbreviations

MIF	molecular interaction field
PLS	partial least squares
QSAR	quantitative structure activity relationship
ECM	extracellular matrix
VEGFR2	vascular endothelial growth factor receptor-2
VEGF	vascular endothelial growth factor
GA	genetic algorithm
CPH	common pharmacophore hypothesis
PC	principal component
CV	cross validation
HUVEC	human umbilical vein endothelial cell
HBA	hydrogen bond acceptor
HBD	hydrogen bond donor
AR	aromatic ring
H	hydrophobic group
PI	positive ionizable
NI	negative ionizable
SAS	solvent-accessible surface

Author Manuscript Author Manuscript Author Manuscript Author Manuscript

References

[1]. Jacobs Jack. “Combating cardiovascular disease with angiogenic therapy.” Drug discovery today 1223 (2007): 1040–1045. [PubMed: 18061883]

[2]. Stupack Dwayne G., and Cheresh David A. “ECM remodeling regulates angiogenesis: endothelial integrins look for new ligands.” Sci. STKE 2002119 (2002): pe7–pe7.

[3]. Lemmon Mark A., and Schlessinger Joseph. “Cell signaling by receptor tyrosine kinases.” Cell 1417 (2010): 1117–1134. [PubMed: 20602996]

[4]. Simons Michael, Gordon Emma, and Claesson-Welsh Lena “Mechanisms and regulation of endothelial VEGF receptor signalling.” Nature Reviews Molecular Cell Biology 1710 (2016): 611–625. [PubMed: 27461391]

[5]. Zachary Ian, et al. “Vascular protection.” Arteriosclerosis, Thrombosis, and Vascular Biology 206 (2000): 1512–1520.

[6]. Horowitz Jeffrey R., et al. “Vascular endothelial growth factor/vascular permeability factor produces nitric oxide-dependent hypotension.” Arteriosclerosis, thrombosis, and vascular biology 1711 (1997): 2793–2800.

[7]. Shiojima Ichiro, et al. “Disruption of coordinated cardiac hypertrophy and angiogenesis contributes to the transition to heart failure.” Journal of Clinical Investigation 1158 (2005): 2108. [PubMed: 16075055]

[8]. Izumiya Yasuhiro, et al. “Vascular endothelial growth factor blockade promotes the transition from compensatory cardiac hypertrophy to failure in response to pressure overload.” Hypertension 475 (2006): 887–893. [PubMed: 16567591]

[9]. Sugimoto Hikaru, et al. “Neutralization of circulating vascular endothelial growth factor (VEGF) by anti-VEGF antibodies and soluble VEGF receptor 1 (sFlt-1) induces proteinuria.” Journal of Biological Chemistry 27815 (2003): 12605–12608. [PubMed: 12538598]

[10]. Eremina Vera, et al. “Glomerular-specific alterations of VEGF-A expression lead to distinct congenital and acquired renal diseases.” Journal of Clinical Investigation 1115 (2003): 707. [PubMed: 12618525]

[11]. Kamba Tomomi, et al. “VEGF-dependent plasticity of fenestrated capillaries in the normal adult microvasculature.” American Journal of Physiology-Heart and Circulatory Physiology 2902 (2006): H560–H576. [PubMed: 16172168]

[12]. Madeddu Paolo. “Therapeutic angiogenesis and vasculogenesis for tissue regeneration.” Experimental physiology 903 *(2005):* 315–326. [PubMed: 15778410]

[13]. Zachary Ian, and Morgan Robert. “Therapeutic angiogenesis for cardiovascular disease: biological context, challenges, prospects.” Heart (2010): hrt-2009.

[14]. Annex Brian H. “Therapeutic angiogenesis for critical limb ischaemia.” Nature Reviews Cardiology 107 (2013): 387. [PubMed: 23670612]

[15]. Hammond H.Kirk, and McKiman M. Dan “Angiogenic gene therapy for heart disease: a review of animal studies and clinical trials.” Cardiovascular research 493 (2001): 561–567. [PubMed: 11166269]

[16]. Simons Michael, et al. “Clinical trials in coronary angiogenesis: issues, problems, consensus.” Circulation 10211 (2000): e73–e86. [PubMed: 10982554]

[17]. Khurana Rohit, and Simons Michael. “Insights from angiogenesis trials using fibroblast growth factor for advanced arteriosclerotic disease.” Trends in cardiovascular medicine 133 (2003): 116–122. [PubMed: 12691676]

[18]. Losordo Douglas W., and Dimmeler Stefanie. “Therapeutic angiogenesis and vasculogenesis for ischemic disease.” Circulation 10922 (2004): 2692–2697. [PubMed: 15184293]

[19]. Ng Yin-Shan, and D’Amore Patricia A. “Therapeutic angiogenesis for cardiovascular disease.” Trials 26 (2001): 278.

[20]. Post Mark J., et al. “Therapeutic angiogenesis in cardiology using protein formulations.” Cardiovascular research 493 *(2001):* 522–531. [PubMed: 11166265]

[21]. Syed Imran S., Sanborn Timothy A., and Rosengart Todd K. “Therapeutic angiogenesis: a biologic bypass.” Cardiology 1011–3 (2004): 131–143. [PubMed: 14988635]

Author Manuscript Author Manuscript Author Manuscript Author Manuscript

[22]. Epstein Stephen E., et al. “Therapeutic interventions for enhancing collateral development by administration of growth factors: basic principles, early results and potential hazards.” Cardiovascular research 493 (2001): 532–542. [PubMed: 11166266]

[23]. Rissanen Tuomas T., and Yla-Herttuala Seppo “Current status of cardiovascular gene therapy.” Molecular Therapy 157 (2007): 1233–1247. [PubMed: 17505481]

[24]. Henry Timothy D., et al. “Intracoronary administration of recombinant human vascular endothelial growth factor to patients with coronary artery disease.” American heart journal 1425 (2001): 872–880. [PubMed: 11685177]

[25]. Hendel Robert C., et al. “Effect of intracoronary recombinant human vascular endothelial growth factor on myocardial perfusion.” Circulation 1012 (2000): 118–121. [PubMed: 10637195]

[26]. Isner Jeffrey M., et al. “Treatment of thromboangiitis obliterans (Buerger’s disease) by intramuscular gene transfer of vascular endothelial growth factor: preliminary clinical results.” Journal of vascular surgery 286 (1998): 964–975. [PubMed: 9845647]

[27]. Makinen Kimmo, et al. “Increased vascularity detected by digital subtraction angiography after VEGF gene transfer to human lower limb artery: a randomized, placebo-controlled, double-blinded phase II study.”Molecular Therapy 61 (2002): 127–133. [PubMed: 12095313]

[28]. Selvaprithviraj Vignesh, et al. “Pro-angiogenic Molecules for Therapeutic Angiogenesis.” Current medicinal chemistry 2431 (2017): 3413–3432. [PubMed: 28738773]

[29]. Talele Tanaji T., Khedkar Santosh A., and Rigby Alan C. “Successful applications of computer aided drug discovery: moving drugs from concept to the clinic.” Current topics in medicinal chemistry 101 (2010): 127–141. [PubMed: 19929824]

[30]. Furet Pascal, et al. “Identification of a new chemical class of potent angiogenesis inhibitors based on conformational considerations and database searching.” Bioorganic & medicinal chemistry letters 1318 (2003): 2967–2971. [PubMed: 12941313]

[31]. Pasha FA, et al. “Pharmacophore and docking-based combined in-silico study of KDR inhibitors.” Journal of Molecular Graphics and Modelling 281 (2009): 54–61. [PubMed: 19447057]

[32]. Lee Kyungik, et al. “Pharmacophore modeling and virtual screening studies for new VEGFR-2 kinase inhibitors.” European journal of medicinal chemistry 4511 (2010): 5420–5427. [PubMed: 20869793]

[33]. Harmange Jean-Christophe, et al. “Naphthamides as novel and potent vascular endothelial growth factor receptor tyrosine kinase inhibitors: design, synthesis, and evaluation.” Journal of Medicinal Chemistry 51 (2008): 1649–1667. [PubMed: 18324761]

[34]. Wang Junmei, et al. “Development and testing of a general amber force field.” Journal of computational chemistry 259 (2004): 1157–1174. [PubMed: 15116359]

[35]. Wang Junmei, et al. “Automatic atom type and bond type perception in molecular mechanical calculations.” Journal of molecular graphics and modelling 252 (2006): 247–260. [PubMed: 16458552]

[36]. Pettersen Eric F., et al. “UCSF Chimera—a visualization system for exploratory research and analysis.” Journal of computational chemistry 2513 (2004): 1605–1612. [PubMed: 15264254]

[37]. Wolber G, Langer T. “LigandScout: 3-D pharmacophores derived from protein-bound ligands and their use as virtual screening filters.” J. Chem. Inf Model 45(1) (2004): 160–169.

[38]. Csizmadia P “MarvinSketch and MarvinView: molecule applets for the World Wide Web.” Proceedings of ECSOC-3, The Third International Electronic Conference on Synthetic Organic Chemistry, September 1ą30. 1999.

[39]. Cereto-Massague Adria, et al. “DecoyFinder: an easy-to-use python GUI application for building target-specific decoy sets.” Bioinformatics 2812 (2012): 1661–1662. [PubMed: 22539671]

[40]. Morris GM, Goodsell DS, Halliday RS, Huey R, Hart WE, Belew RK, Olson AJ “Automated docking using a Lamarckian genetic algorithm and an empirical binding free energy function.” Journal of Computational Chemistry 19 (1998): 1639–1662.

[41]. Abreu Rui, et al. “Selective Flexibility of SideD-Chain Residues Improves VEGFRD-2 Docking Score using AutoDock Vina.” Chemical biology & drug design 794 (2012): 530–534. [PubMed: 22188672]

[42]. Discovery Studio 4.0 is a product of Accelrys Inc, San Diego, CA, USA.

Author Manuscript Author Manuscript Author Manuscript Author Manuscript

[43]. Tosco Paolo and Balle Thomas. “Open3DQSAR: a new open-source software aimed at high-throughput chemometric analysis of molecular interaction fields.” Journal of Molecular Modeling 17 (2011): 201–208. [PubMed: 20383726]

[44]. Roy Kunal, and Mitra Indrani. “On various metrics used for validation of predictive QSAR models with applications in virtual screening and focused library design.” Combinatorial chemistry & high throughput screening 146 (2011): 450–474. [PubMed: 21521150]

[45]. The PyMOL Molecular Graphics System, Version 2.0 Schrodinger, LLC.

Author Manuscript Author Manuscript Author Manuscript Author Manuscript

Highlights

1. Four natural VEGFR2-binding leads identified by ligand-based pharmacophore screening.
2. Agnuside has strongest VEGFR2-binding energy profile of leads: −11.3 kcal/M affinity.
3. Agnuside possesses 1.376 g/mL EC_{50} for HUVEC proliferation.
4. Agnuside promotes HUVEC tubulogenesis dose-dependently.
5. SAR of agnuside and naphthyl derivatives established by chemometric analysis of MIFs.

Author Manuscript Author Manuscript Author Manuscript Author Manuscript

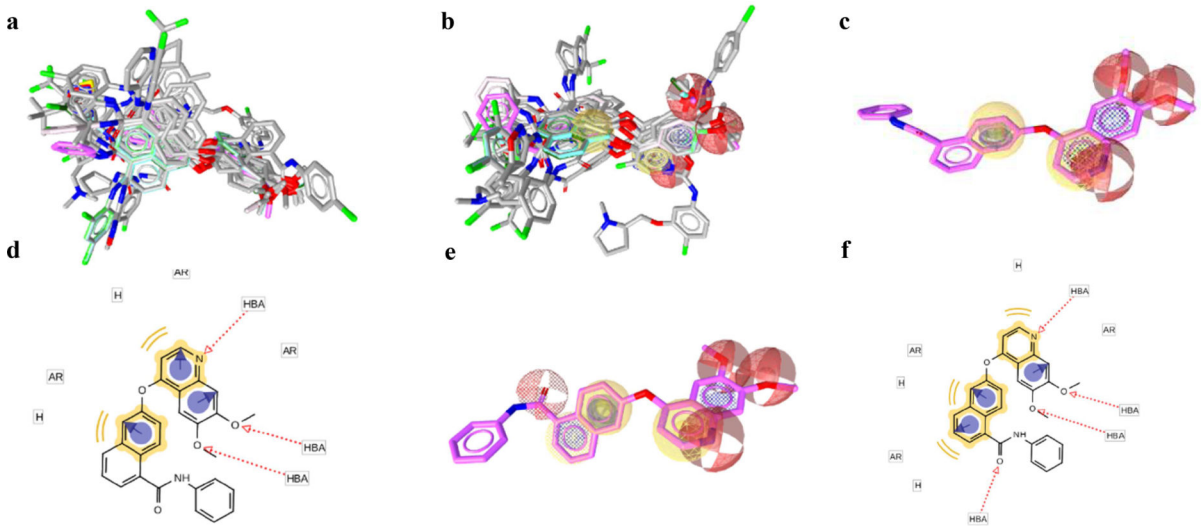

Figure 1 |. Characterization of required physicochemical and steric properties required for VEGFR2-naphthamide binding by CPH construction.

a, b, Conformational alignment derived from atom-based molecular superpositioning of training set molecules with NAPH1 as template structure (**a**) fitted to *CPH1* (**b**). **c-f,** 3D (**c, e**) and 2D (**d, f**) representations of *CPH1* (**c, d**) and *CPH4* (**e, f**) substructure-based pharmacophore models aligned with molecular-docking acquired bioactive structure of NAPH1. The directionality of each of the chemical vectors is depicted in 2D-representation. Chemical features are depicted as follows: hydrogen bond acceptors as red spheres, aromatic ring groups as blue spheres, and hydrophobic groups as yellow spheres. NAPH1 shown in stick model. Exclusion volumes are not shown.

Author Manuscript Author Manuscript Author Manuscript Author Manuscript

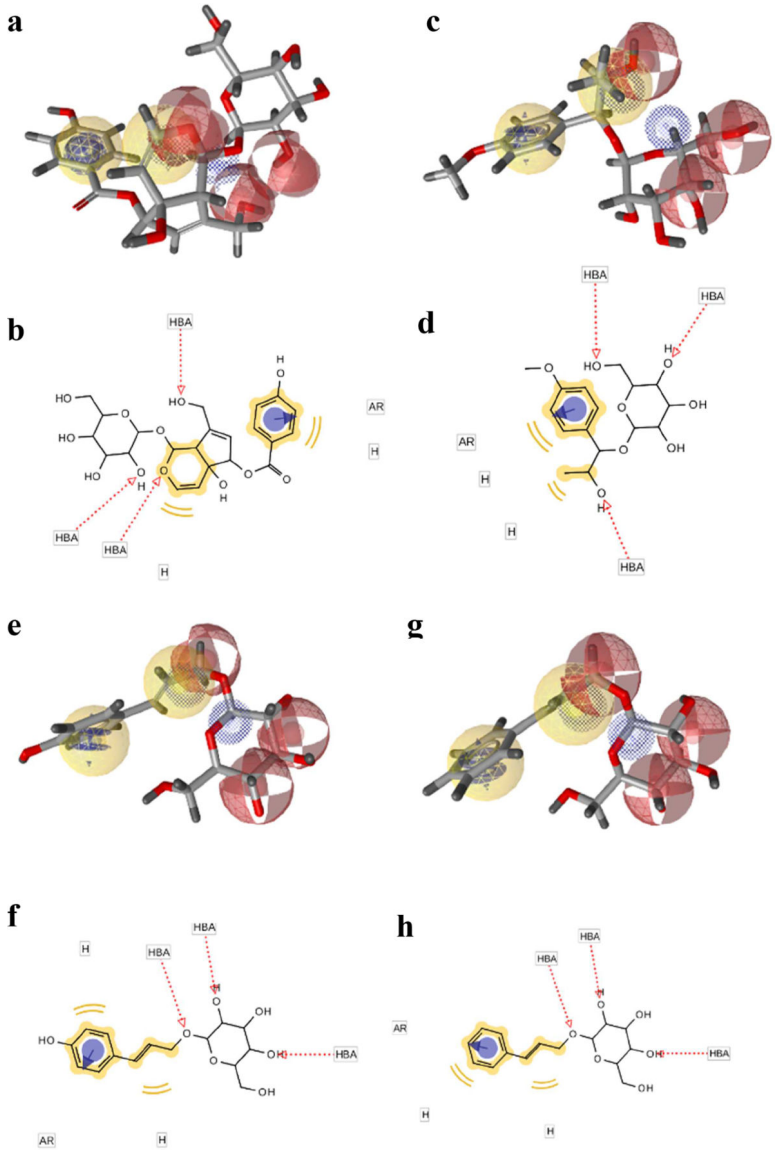

Figure 2 |. Ligand-based virtual screening resulted in identification of lead small molecules possessing similar chemical, structural, and steric properties as *CPH1*.

a-h, Comparison of pharmacophoric overlap of agnuside (**a, b**), erythro- anethole glycol 1-glucoside (**c, d**), sachaliside (**e, f**), and rosin (**g, h**) with *CPH1.* Lead molecules shown as stick models. Exclusion volumes are not shown.

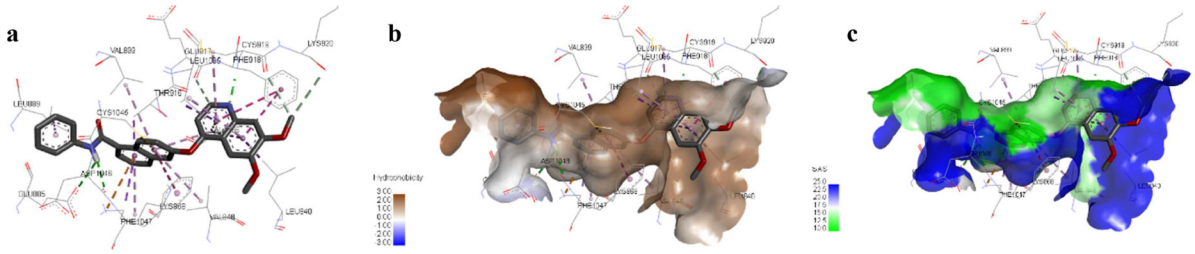

Figure 3 |. Binding interaction mechanisms between scaffold A naphthamides and VEGFR2 are influenced by H-bonding and hydrophobic network formation with front pocket, tunnel region, and hydrophobic back pocket.

a-c, Bioactive conformation of NAPH1 within VEGFR2 binding cleft (**a**) with reference hydrophobicity receptor surface potential map calculated using hydrophobic probe atoms and measured on −3.0 to +3.0 scale (**b**) and with a reference solvent-accessible surface (SAS) receptor potential map measured on a +10.0 to +25.0 scale (**c**). Brown, white, and blue denote receptor surface areas of high, neutral, and low hydrophobicity, respectively. Blue and green denote regions of solvent-accessibility and inaccessibility, respectively. Hydrophobic interactions are shown as purple dotted lines. Hydrogen bond donator and acceptor interactions are shown as dark green dotted lines. Cation-π electrostatic interactions are shown as orange dotted lines. π-π stacking interactions are shown as yellow dotted lines. Images from Discovery Studio Client 4.0.

Author Manuscript Author Manuscript Author Manuscript Author Manuscript

Author Manuscript Author Manuscript Author Manuscript Author Manuscript

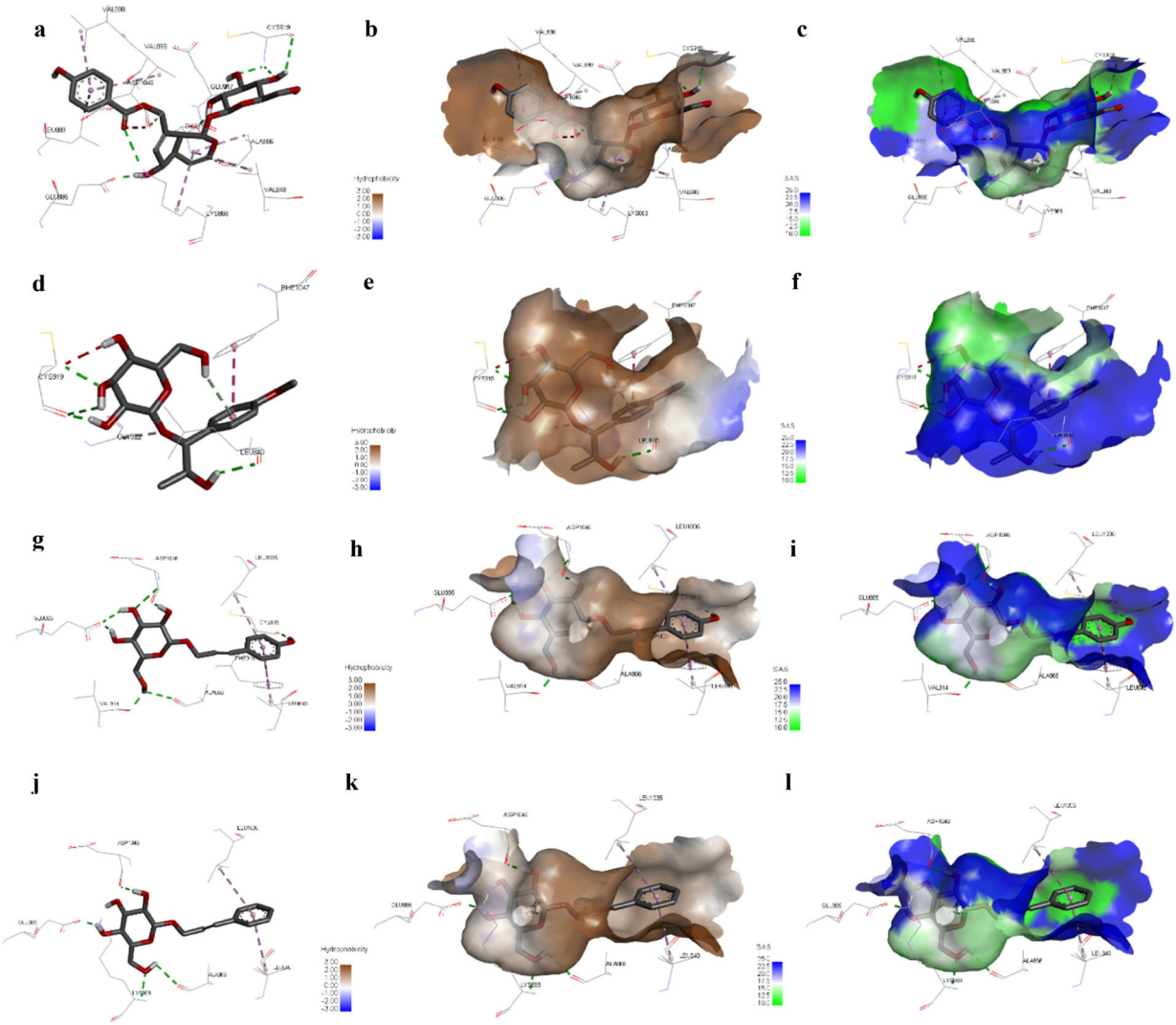

Figure 4 |. Mapping hydrophobicity and SAS receptor surface potential maps onto VEGFR2-lead molecule complexes indicates agnuside forms strong hydrophobic and hydrogen bond networks in front and back pockets of VEGFR2.

a, d, g, j, Molecular docking complexes of VEGFR2 with energetically favorable conformations of agnuside (**a**), erythro-anethole glycol 1-glucoside (**d**), sachaliside (**g**), and rosin (**j**). **b, e, h, k,** Hydrophobicity receptor surface potential measured on a −3.00 to +3.00 scale mapped onto docked complexes of agnuside (**b**), erythro-anethole glycol 1-glucoside (**e**), sachaliside (**h**), and rosin (**k**). Brown, white, and blue denote receptor surface areas of high, neutral, and low hydrophobicity, respectively. **c, f, i, l,** VEGFR2- agnuside (**c**), VEGFR2-erythro-athenole (**f**), VEGFR2-sachaliside (**i**), and VEGFR2-rosin (**l**) complexes with reference SAS receptor potential maps measured on a +10.0 to +25.0 scale. Blue and green denote regions of solvent-accessibility and solvent-inaccessibility, respectively. Hydrophobic interactions are shown as purple dotted lines. Hydrogen bond donator and acceptor interactions are shown as dark green dotted lines. Cation-n electrostatic interactions are shown as orange dotted lines. n-n stacking interactions are shown as yellow dotted lines. Images from Discovery Studio Client.

Author Manuscript Author Manuscript Author Manuscript Author Manuscript

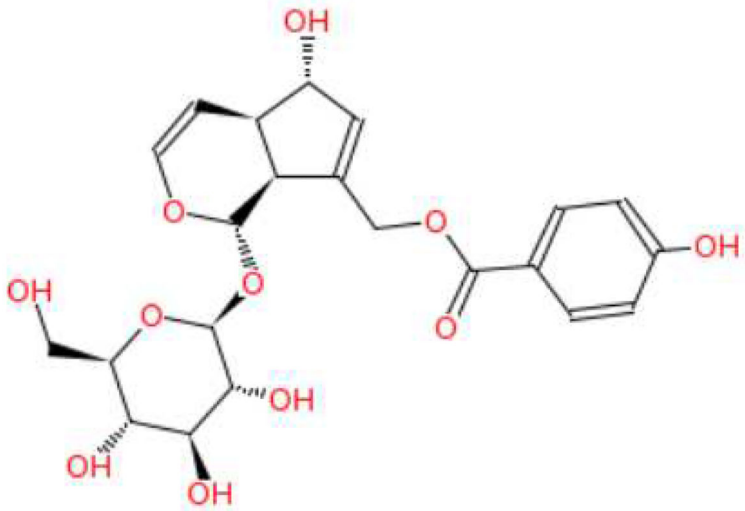

Figure 5 |. 2D chemical structure of agnuside.

Author Manuscript Author Manuscript Author Manuscript Author Manuscript

a

Compound	BA	BA_{calc}		
		$EC_{30.0}$	$EC_{20.0}$	$C_{40.0}$
1	15.00	14.97	15.02	15.01
2	12.13	12.39	12.44	12.47
3	9.750	9.761	9.726	9.727
4	14.78	14.71	14.67	14.68
5	14.58	14.64	14.61	14.61
6	14.28	14.07	14.13	14.12
7	10.48	10.33	10.33	10.32
8	12.82	12.74	12.80	12.77
9	14.83	14.97	14.86	14.98
10*	14.33	14.66	14.62	14.61
11*	12.05	12.33	12.21	12.28
12	12.98	12.95	12.91	12.90
13	13.20	13.55	13.56	13.61
14	14.26	14.41	14.43	14.43
15*	13.73	13.82	13.84	13.88
16	14.83	14.70	14.62	16.66
17	12.84	12.76	12.78	12.77
18	15.17	15.26	15.26	15.21
19	15.14	15.13	15.10	15.09

b

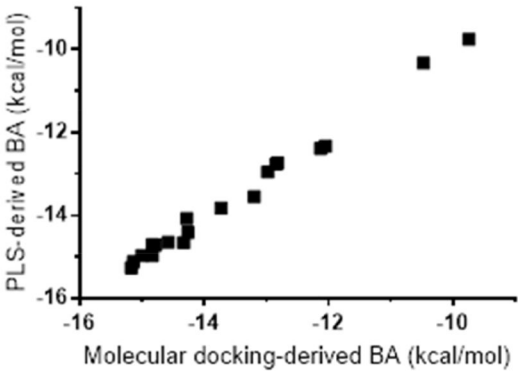

Figure 6 |. QSAR model with 30.0 kcal/mol energy cutoff and 3 PCs resulted in strongest PLS regression of binding affinity.

a, PLS-derived binding affinities of QSAR training and test set molecules for 3 PC extraction at 20.0, 30.0, and 40.0 kcal/mol energy cutoffs. BA, binding affinity calculated by docking. BA_{calc}, binding affinity from PLS analysis. Binding affinities are in kcal/mol. * denotes test set molecules, **b**, Molecular docking-derived vs. PLS-derived binding affinities for 3 PCs and 30.0 kcal/mol energv cutoff.

Author Manuscript Author Manuscript Author Manuscript Author Manuscript

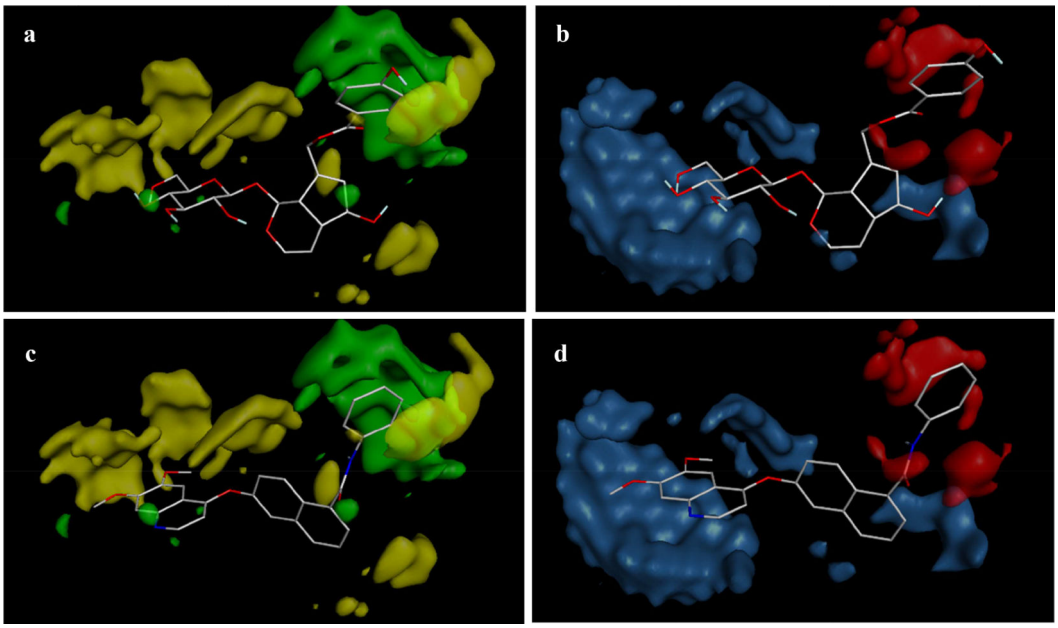

Figure 7 |. Identification of potential structural and chemical modifications of agnuside to improve VEGFR2 binding affinity.

a-d, QSAR-derived coefficient contour maps of steric and electrostatic MIFs defining naphthamide-VEGFR2 interactions with bioactive conformations of agnuside (**a, b**) and NAPH1 (**c, d**). Isosurf values for steric and electrostatic MM fields are ±0.0003 and ±0.0001, respectively. Green and yellow contours represent regions where steric bulkiness increases and reduces binding affinity, respectively. Blue and red contours represent regions where electropositive species increase and reduce binding affinity, respectively. Images from PyMOL. *1.5 column width*

Author Manuscript Author Manuscript Author Manuscript Author Manuscript

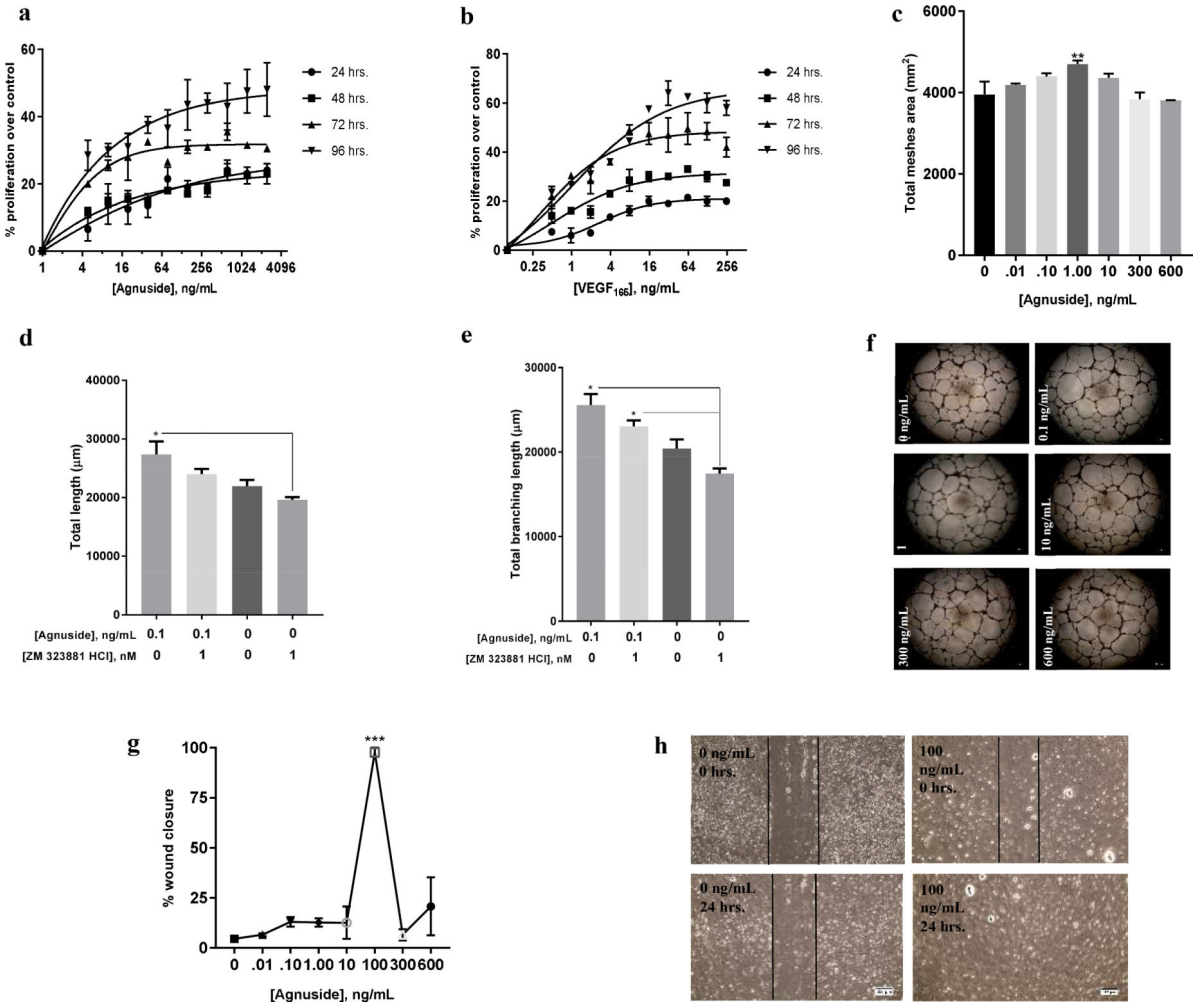

Figure 8 |. Agnuside promotes HUVEC proliferation, tube formation, and scratch wound migration and may actively compete with ZM 323881 HCl.

a, b, Percent proliferation over control of HUVECs treated with different concentrations of agnuside (1–2500 ng/mL) (**a**) and VEGF (0.1–250 ng/mL) (**b**) in EBM complete media at 24–96 hr. time points fitted with dose- dependent stimulation curves with normalized response and variable slope. **c,** Total meshes area of tubular networks formed by HUVECs treated with 0–600 ng/mL agnuside 22 hrs. after seeding. Total meshes area was calculated with ImageJ. Statistical significance determined by one-way Dunnett's multiple comparisons test. **d**, **e,** Total length (**d**) and total branching length (**e**) of tubular networks formed by HUVECs treated with 0.1 ng/mL agnuside alone, 0.1 ng/mL agnuside plus 1 nM ZM 323881 HCl, and 1 nM ZM 323881 HCl alone. Total length and total branching length were calculated with ImageJ. Statistical significance determined by one-way Dunnett's multiple comparisons test. **f**, Representative images (phase-contrast, 4x) of tubular networks formed by HUVECs in presence of 0, 0.1, 1, 10, 300, and 600 ng/mL agnuside at 22 hrs. Scale bars, 500 µm. **g,** Percentage wound closure for HUVECs treated with 0.01–600 ng/mL agnuside 24 hrs. after linear scratch application. Statistical significance determined by Dunnett's multiple comparisons test. **h,** Representative images (phase-contrast, 10x) of initial scratch wound distance (top) and extent of migration after 24 hrs. (bottom) in presence of 0 ng/mL

Author Manuscript Author Manuscript Author Manuscript Author Manuscript

agnuside (left) and 100 ng/mL agnuside (right). Scratch wound distance is given by black lines. Scale bars, 500 μm. All data values represent the mean±SEM of two biological replicates. *$p<0.05$.

Author Manuscript Author Manuscript Author Manuscript Author Manuscript

Table 1|

Structural features of training and test set naphthyl-based derivatives used for merged-feature, ligand-based CPH development. Shown beside each naphthamide (training set: NAPH1–6 and test set: NAPH7–29) is its corresponding starting structural scaffold (A-C) and the chemical substituent at its R_1/R_2 positions. Note that scaffolds B and C only possess an R_1 group.

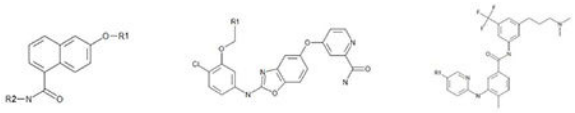

A B C

Compound	Scaffold	Substituents	
		R_1	R_2
Training Set			
NAPH1 *	A	−6,7-dimethoxyquinoline	phenyl
NAPH2	A	−6,7-dimethoxyquinoline	4-methylphenyl
NAPH3	A	−6,7-dimethoxyquinoline	3-chlorophenyl
NAPH4	A	−6,7-dimethoxyquinoline	3,5-dichlorophenyl
NAPH5	A	−6,7-dimethoxyquinoline	3-isoxazole
NAPH6	A	−6,7-dimethoxyquinoline	4-chlorophenyl
Test Set			
NAPH7	A	−6,7-dimethoxyquinoline	4-(trifluoromethyl)phenyl
NAPH8	A	−6,7-dimethoxyquinoline	4-fluorophenyl
NAPH9	A	−6,7-dimethoxyquinoline	2-thiazolyl
NAPH10	A	−3-fluoro-6,7-dimethoxyquinoline	4-chlorophenyl
NAPH11	B	−1-methylpyrrolidine	--
NAPH12	A	−6-(methylamino)pyrimidine	4-chlorophenyl
NAPH13	A	−7H-pyrrolo[2,3-d]pyrimidine	4-chlorophenyl
NAPH14	A	−7-methoxyquinoline	4-chlorophenyl
NAPH15	A	−6,7-dimethoxyquinazoline	4-chlorophenyl
NAPH16	A	−6,7-dimethoxyquinoline	2,4-dichlorophenyl
NAPH17	A	−6,7-dimethoxyquinoline	4-chloro-3-(trifluoromethyl)phenyl
NAPH18	A	−6,7-dimethoxyquinoline	3-pyridyl
NAPH19	A	−6,7-dimethoxyquinoline	4-pyridyl
NAPH20	A	−6,7-dimethoxyquinoline	5-methyl-3- isoxazolyl
NAPH21	A	−6,7-dimethoxyquinoline	3-methyl-5-isoxazolyl
NAPH22	A	−6,7-dimethoxyquinoline	cyclopropyl
NAPH23	A	-6,7-dimethoxyquinoline	5-*tert*-butyl-3-isoxazolyl
NAPH24	A	−6,7-dimethoxyquinoline	isopropyl
NAPH25	A	−6,7-dimethoxyquinoline	cyclobutyl
NAPH26	A	−6,7-dimethoxyquinoline	1-methylcyclopropyl
NAPH27	A	−6,7-dimethoxyquinoline	propyl
NAPH28	A	−6,7-dimethoxyquinoline	cyclopentyl

Author Manuscript Author Manuscript Author Manuscript Author Manuscript

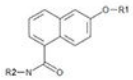

A

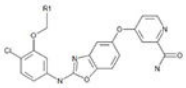

B

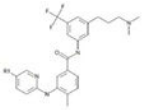

C

Compound	Scaffold	Substituents	
		R_1	R_2
NAPH29	C	−3-pyrimidine	--

*denotes that the compound was used as the template for molecular superpositioning of the training set.

Author Manuscript Author Manuscript Author Manuscript Author Manuscript

Table 2|

Statistical evaluation of pharmacophoric specificity by decoy set external validation. Chemical features and test- set derived normalized pharmacophoric fit scores of generated CPHs and statistical parameters obtained from external 2D- descriptor based decoy set validation. Enrichment factor was calculated with the following formula: $(H_a/H_t)/(A/D)$ and percentage ratio of active was calculated by (H_a/A), where H_t is the total number of molecules in the hit list, H_a is the total number of active molecules present in hit list, A is the total number of active molecules in the decoy set database, and D is total number of molecules present in decoy set. **AR**, aromatic ring group. **H**, hydrophobic group. **HBA**, hydrogen bond acceptor.

Pharm. Name	Features	Pharm. Fit Score	Enrichment factor (*E*)	% Ratio of actives
CPH1	3 **AR,** 2 **H,** 3 **HBA**	0.884	0.891	56.3
CPH2	3 **AR**, 2 **H,** 3 **HBA**	0.877	0.766	6.25
CPH3	3 **AR**, 2 **H,** 3 **HBA**	0.869	0.781	12.5
CPH4	3 **AR**, 3 **H,** 4 **HBA**	0.819	0.844	37.5
CPH5	1 **AR**, 2 **H,** 4 **HBA,** 1 **HBD**	0.790	0.828	31.3

Author Manuscript

Author Manuscript

Author Manuscript

Author Manuscript

Table 3|

Identification of VEGFR2-binding lead molecules by virtual screening. Matching features and pharmacophoric fit scores of lead molecules and *CPH1.* Fit score measured by structural and chemical similarities. *Erythro,* erythro-anethole glycol 1-glucoside. **AR**, aromatic ring group. **H**, hydrophobic group. **HBA**, hydrogen bond acceptor.

Lead molecule	Matching Features	*CPH1* Fit Score
Agnuside	1 **AR,** 2 **H,** 3 **HBA**	66.82
Erythro	1 **AR**, 2 **H,** 3 **HBA**	66.74
Sachaliside	1 **AR**, 2 **H,** 3 **HBA**	65.98
Rosin	1 **AR**, 2 **H,** 3 **HBA**	65.97

Author Manuscript Author Manuscript Author Manuscript Author Manuscript

Table 4|

Binding free energy calculations and hydrophobic network formation of VEGFR2-docked complexes indicate the strong conformational stability of agnuside within binding cleft. Total binding free energy components of docked complexes of scaffold A training and test set naphthamides and lead molecules calculated from Lamarckian GA scoring parameters. Distances of hydrophobic interactions between small molecules and catalytically important residues in VEGFR2's binding site. - denotes the absence of the hydrophobic interaction. Erythro, erythro-anethole glycol 1-glucoside.

Complex	$E_{binding(kcal/mol)}$	$E_{electrostatic(kcal/mol)}$	$E_{vdw+Hbond+desolv(kcal/mol)}$	$E_{total\ internal\ (kcal/mol)}$	-Leu889$_{(hydrophobic,\ A)}$	-Val899$_{(hydrophobic,\ A)}$	-Val848$_{(hydrophobic,\ A)}$	-Ala866$_{(hydrophobic,\ A)}$
NAPH1	−15.00	−0.03	−12.64	−3.68	4.83	4.85	4.95	3.60
NAPH2	−12.13	−0.04	−10.71	−2.76	3.48	4.72	3.51	3.81
NAPH3	−9.750	+0.01	−7.550	−3.74	−	5.38	4.49	4.68
NAPH4	−14.78	+0.02	−12.49	−3.60	3.80	4.85	4.89	4.14
NAPH5	−14.58	−0.05	−12.32	−3.65	3.73	5.08	4.89	3.65
NAPH6	−14.28	+0.03	−10.53	−2.02	4.04	5.43	4.30	4.34
NAPH7	−12.82	+0.01	−10.90	−3.66	3.56	5.09	4.56	4.34
NAPH8	−10.48	−0.01	−8.730	−3.26	−	5.01	5.02	3.47
NAPH9	−14.83	−0.20	−12.77	−3.33	4.85	5.03	4.91	3.53
NAPH10	−14.33	−0.03	−13.13	−2.65	5.02	5.30	4.66	3.60
NAPH11	−12.05	+0.19	−10.78	−3.38	3.44	4.92	−	4.22
NAPH12	−12.98	+0.01	−10.93	−3.16	4.56	5.02	4.69	4.15
NAPH13	−13.20	−0.26	−11.16	−2.71	3.60	-	4.54	4.05
NAPH14	−14.26	−0.15	−12.17	−3.16	3.65	5.37	4.65	3.47
NAPH15	−13.73	−0.02	−11.62	−3.49	3.66	5.09	4.61	3.88
NAPH16	−14.83	−0.05	−13.05	−3.16	3.97	5.19	4.50	4.27
NAPH17	−12.84	0.00	−12.00	−2.52	4.60	5.12	4.42	4.34
NAPH18	−15.17	−0.07	−13.10	−3.55	5.19	5.03	4.98	3.41
NAPH19	−15.41	−0.11	−13.21	−3.59	3.91	5.15	4.83	3.43
Agnuside	−11.28	−0.08	−9.630	−4.31	3.63	5.44	4.89	4.25
Sachaliside	−9.270	+0.03	−7.590	−3.52	-	-	-	-
Erythro	−6.460	−0.11	−4.840	−4.53	-	-	-	-
Rosin	−9.740	+0.18	−7.370	−4.20	-	-	-	-

Author Manuscript Author Manuscript Author Manuscript Author Manuscript

Table 5|

Statistical parameters from cross-validated and non cross-validated PLS analyses of QSAR-derived models elucidating binding affinity-physicochemical property relationships of naphthamides. Statistics include r^2, non cross-validated correlation coefficient, F, F-test value, r_{pred}^2, non cross-validated correlation coefficient of test set, SDEP, standard deviation of error of prediction of binding affinities for the non-cross validated calculations, q_{loo}^2, cross- validated correlation coefficient for leave-one-out strategy, q_{lto}^2, cross-validated correlation coefficient for leave-two-out strategy, q_{lmo}^2, cross-validated correlation coefficient for leave-multiple-out strategy, r_{test}^2, cross-validated correlation coefficient for test set, and $SDEP_{test}$, standard deviation of error of prediction of test set binding affinities for cross- validated calculations. Calculated statistics for PLS extraction of 1–6 PCs and for 20.0, 30.0, and 40.0 kcal/mol pretreatment energy cutoff values.

EC: 20.0 kcal/mol									
PC	r^2	F	r_{pred}^2	SDEP	q_{loo}^2	q_{lto}^2	q_{lmo}^2	r_{test}^2	$SDEP_{test}$
1	0.751	42.3	0.582	0.639	0.683	0.656	0.648	0.886	0.334
2	0.872	44.4	0.862	0.368	0.774	0.741	0.725	0.950	0.222
3	0.961	99.4	0.981	0.136	0.761	0.737	0.722	0.956	0.207
4	0.991	310	0.826	0.412	0.761	0.737	0.720	0.913	0.291
5	0.995	407	0.857	0.374	0.763	0.734	0.720	0.927	0.267
6	0.997	505	0.890	0.329	0.764	0.740	0.723	0.956	0.207
EC: 30.0 kcal/mol									
PC	r^2	F	r_{pred}^2	SDEP	q_{loo}^2	q_{lto}^2	q_{lmo}^2	r_{test}^2	$SDEP_{test}$
1	0.750	42.1	0.572	0.647	0.708	0.681	0.672	0.874	0.352
2	0.873	44.6	0.852	0.380	0.783	0.751	0.737	0.958	0.202
3	0.961	98.2	0.979	0.142	0.777	0.753	0.736	0.933	0.256
4	0.992	321	0.837	0.400	0.776	0.749	0.732	0.908	0.299
5	0.995	426	0.867	0.361	0.768	0.745	0.732	0.925	0.271
6	0.997	543	0.896	0.319	0.778	0.753	0.735	0.952	0.217
EC: 40.0 kcal/mol									
PC	r^2	F	r_{pred}^2	SDEP	q_{loo}^2	q_{lto}^2	q_{lmo}^2	r_{test}^2	$SDEP_{test}$
1	0.755	43.0	0.579	0.642	0.676	0.648	0.641	0.870	0.356
2	0.873	44.6	0.853	0.379	0.764	0.729	0.715	0.943	0.235
3	0.960	97.1	0.978	0.147	0.744	0.720	0.707	0.950	0.222
4	0.991	301	0.820	0.419	0.746	0.719	0.702	0.891	0.326
5	0.995	397	0.852	0.380	0.736	0.714	0.702	0.906	0.304
6	0.997	500	0.882	0.340	0.749	0.723	0.704	0.937	0.248